COMMUNICATION

Check for updates

Shear-structured $MoNb_6O_{18}$ as a new anode for lithium-ion batteries†

Jialin Cheng, Fengqi Lu [ID]* and Xiaojun Kuang [ID]

Owing to their high theoretical capacities, safe operational voltage, unique tunnel-shaped structural features for fast lithium ion transfer, and structural stability, niobium-based oxides are regarded as promising candidate anode materials for lithium-ion batteries (LIBs). Here, molybdenum niobium oxide ($MoNb_6O_{18}$) with a high theoretical capacity of 399 mA h g^{-1} (Mo^{6+}/Mo^{4+} and Nb^{5+}/Nb^{3+}) was developed as a new anode material for LIBs. The crystal structure of $MoNb_6O_{18}$ was observed to display a Wadsley–Roth phase of the ReO_3 shear structure. The discharge capacity of micron-sized particles of $MoNb_6O_{18}$ was measured to be 219.4 mA h g^{-1} with a high initial Coulombic efficiency of 96.8% at 0.2C and 154.3 mA h g^{-1} at 1C from 1.0 to 3.0 V. The results of *ex situ* X-ray diffraction (XRD) experiments revealed the ability of $MoNb_6O_{18}$ to serve as an intercalation-type anode material for lithium ion storage with outstanding structural stability. Also, an $LiMn_2O_4//MoNb_6O_{18}$ full cell displayed desirable lithium-ion storage properties.

Introduction

Lithium-ion batteries (LIBS), as the most popular energy storage device, are widely used in various fields such as mobile electronics products, grid storage, and even in electric vehicles (EVs).[1–6] Graphite, as the prevailing anode for commercial LIBs, has a high theoretical capacity (372 mA h g^{-1}). However, its use could result in lithium plating or the formation of lithium dendrites when working at high charging/discharging rates and at low potentials, and thus has safety concerns.[7–10] It has been found that TiO_2,[11] $Li_4Ti_5O_{12}$,[12] $LiCrTiO_4$[13] and other titanium-based materials are suitable for use as anode materials for LIBs

Key Laboratory of New Processing Technology for Nonferrous Metal & Materials, Ministry of Education Guangxi Key Laboratory of Optical and Electronic Materials and Devices, College of Materials Science and Engineering, Guilin University of Technology, Guilin 541004, P. R. China. E-mail: lufengqi@glut.edu.cn
† Electronic supplementary information (ESI) available. See DOI: 10.1039/d1ma00590a
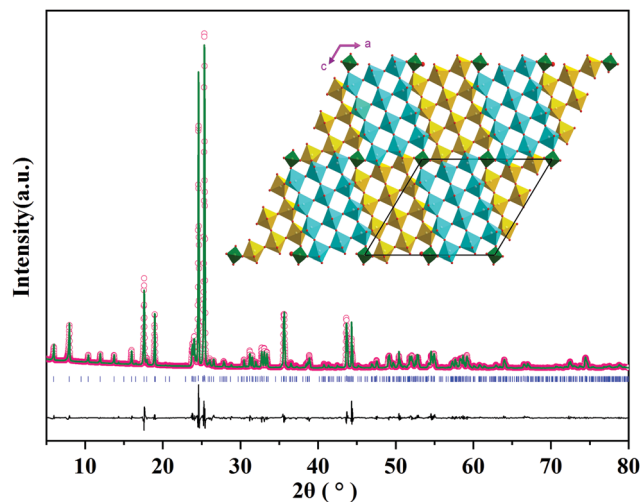
with a safe voltage of about 1.55 V. Unfortunately, their disadvantages of low theoretical capacity and low energy density significantly hinder their practical applications in next-generation LIBs requiring high power density levels and long lifespans.[14–16] Therefore, it is urgent to investigate suitable anode materials with safe working potentials and high energy density and cycling stability levels, especially for EVs.[17]

Recently, niobium-based oxides have been extensively investigated as high-rate anode materials for LIBs, due to their high theoretical capacities based on multielectron reactions, fast lithium ion transport, and, most importantly, safe operating voltage (at just above 1.0 V vs. Li^+/Li).[18–20] Therefore, niobium-based oxide anodes are promising candidates for high-power LIB anodes, specifically in EVs.[21] Most niobium-based oxides form the Wadsley–Roth crystallographic shear structure with blocks consisting of distorted MO_6 octahedra sharing corners, and are built of $n \times m \times \infty$ ReO_3-type units (with n and m denoting the numbers of MO_6 octahedra along the length and width of the blocks).[22] This unique open-tunnel structure can promote lithium ion diffusion and enhance lithium storage capacities.[19] Recently, Wadsley–Roth-shear-structured niobium-based oxides, including $W_5Nb_{16}O_{55}$,[23] $MoNb_{12}O_{33}$,[24] $WNb_{12}O_{33}$,[25] $Mo_3Nb_{14}O_{44}$,[26] $W_3Nb_{14}O_{44}$,[27] $TiNb_2O_7$,[28] $Ti_2Nb_{10}O_{29}$,[29] have been investigated as high-rate anode materials for LIBs. Mo–Nb–O oxides with Wadsley–Roth shear structure anode materials have shown great potential for high-rate lithium ion storage. To the best of our knowledge, $MoNb_{12}O_{33}$, $Mo_3Nb_{14}O_{44}$ and $Mo_3Nb_2O_{14}$ are the only three available Mo–Nb-based oxide anode materials. Very few Mo–Nb–O oxides have so far been used as anodes. In the work described here, a new micro-sized Mo–Nb–O oxide ($MoNb_6O_{18}$) particle, one made by tailoring the ratio of Mo to Nb, was investigated as an anode material for LIBs.

Results and discussion

The crystal structure of $MoNb_6O_{18}$ was characterized using X-ray diffraction (XRD). As shown in Fig. 1, sharp diffraction peaks were observed, indicating its good crystallinity. To the

Fig. 1 XRD pattern of $MoNb_6O_{18}$ and the corresponding Rietveld refinement result, with the inset image displaying a view of the crystal structure along the b axis.

Fig. 2 Morphology and microstructure of $MoNb_6O_{18}$. (a) SEM image. (b–d) EDS elemental mapping images for (b) Mo, (c) Nb, and (d) O. (e) SAED pattern. (f) HRTEM image.

best of our knowledge, no crystal structure of $MoNb_6O_{18}$ has been previously reported; and no information about its crystal structure was found in the Inorganic Crystal Structure Database (ICSD) and the International Centre for Diffraction Data (ICDD). Careful analysis of the XRD pattern of $MoNb_6O_{18}$ showed its diffraction characteristics to be very similar to those of $MoTa_{12}O_{33}$. According to this result, $MoNb_6O_{18}$ formed a crystal structure similar to that of $MoTa_{12}O_{33}$, *i.e.*, a monoclinic Wadsley–Roth shear structure in an $I2/m$ space group. An XRD Rietveld refinement was performed using the Wadsley–Roth shear structure of $MoTa_{12}O_{33}$ as the initial structural model; the refinement converged to an R_{wp} of 10.35%, R_p of 7.48%, and R_{Bragg} of 3.32%. The cell lattice parameters of $MoNb_6O_{18}$ were determined to be $a = 17.730(2)$ Å, $b = 3.822(7)$ Å, $c = 19.417(2)$ Å, $\beta = 106.43(6)°$, with a unit-cell volume V of $1260.46(2)$ Å^3. This result confirmed that the as-prepared $MoNb_6O_{18}$ adopted the Wadsley–Roth shear structure with many Nb and O vacancies. As shown in the inset of Fig. 1, 3×4 NbO_6 octahedral blocks were spread to an indefinite extent on the a–c layer, and extended indefinitely along the direction of the b-axis. The 3×4 blocks linked to each other as a result of edge-sharing NbO_6 octahedra, and corner-sharing MoO_4 tetrahedra. The NbO_6 octahedra shared corners with each other within the block, thus providing many vacant sites for lithium ion storage and fast diffusion.[24] The Mo:Nb atomic ratio was determined from an ICP analysis to be 0.95:6, consistent with the theoretical value (1:6) in $MoNb_6O_{18}$ oxide.

The morphology and microstructure of $MoNb_6O_{18}$ samples were observed using scanning electron microscopy (SEM) and transmission electron microscopy (TEM). In the SEM image (Fig. 2a), $MoNb_6O_{18}$ exhibited irregular rod-like particles with a size distribution ranging from 0.3 to 3 μm. The elements Mo, Nb and O were determined to be uniformly distributed in each $MoNb_6O_{18}$ rod-like particle (Fig. 2b–d). The observed bright diffraction spot in the selected-area electron diffraction (SAED) pattern of an $MoNb_6O_{18}$ sample, shown in Fig. 2e, can be well

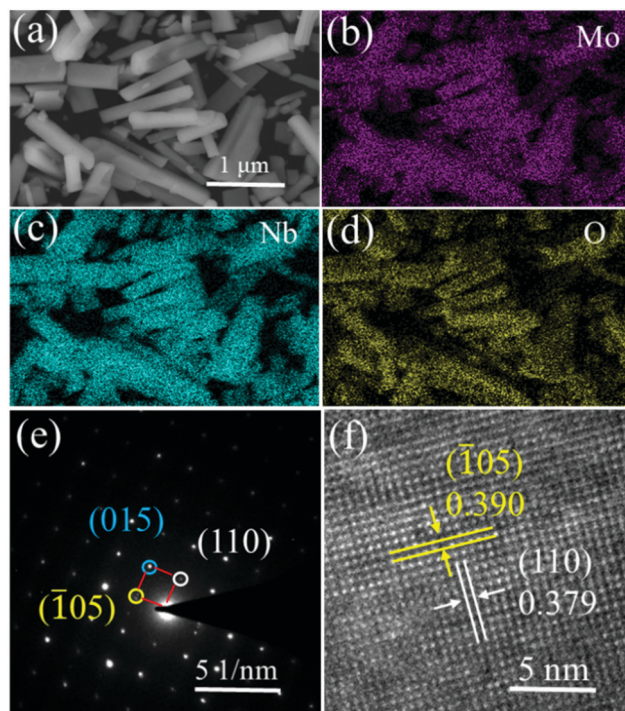indexed to (110), ($\bar{1}05$) and (015) planes of Wadsley–Roth shear structure characteristic of $MoNb_6O_{18}$. The inter-planar distances observed in a high-resolution TEM (HRTEM) image of $MoNb_6O_{18}$, shown in Fig. 2f, were measured to be about 0.390 and 0.379 nm, corresponding to the ($\bar{1}05$) and (110) planes, respectively.

The lithium-ion storage properties of $MoNb_6O_{18}$ electrodes were investigated by taking CV and GCD measurements of them at room temperature. Fig. 3a shows CV curves of $MoNb_6O_{18}$ acquired in different voltage ranges (specifically 0.8–3.0 V, 1.0–3.0 V and 1.2–3.0 V) at a scanning rate of 0.2 mV s^{-1}. During the anodic scanning process, reduction peaks were observed at about 2.28 V (R_1) and 1.92 V (R_2), and could be attributed to conversions of Mo(IV) to Mo(V), and of Mo(V) to Mo(IV).[26] Peaks were also observed at about 1.72 V, and could be ascribed to the reduction of Nb(V) to Nb(IV).[30–32] In addition, peaks were observed at about 1.14 V (R_4), and corresponded to the reduction of Nb(IV) to Nb(III) at the voltage ranges 0.8–3.0 V and 1.0–3.0 V. During the cathodic scanning process, one broad oxidation peak appeared at about 1.88 V. Comparison of CV curves obtained using the three different voltage ranges clearly showed the $MoNb_6O_{18}$ electrode displaying the highest peak current for the voltage range 1.0–3.0 V.

The rate capability and cycling performance of $MoNb_6O_{18}$ were tested at various rates and voltage ranges. Fig. 3b illustrates the rate properties from 0.2 to 5C. In the first cycle at 0.2C, the $MoNb_6O_{18}$ electrode showed the highest discharge capacity of 287.3 mA h g^{-1} at the voltage range 0.8 to 3.0 V, but a rather low charge capacity of 197.7 mA h g^{-1}, which could be
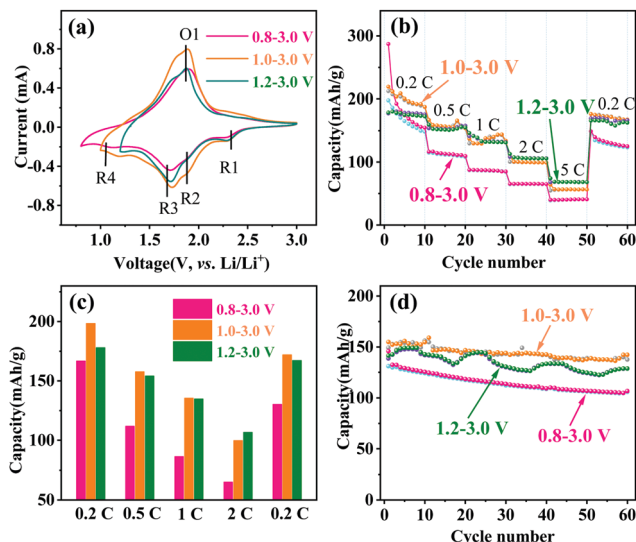
Fig. 3 Electrochemical performances of $MoNb_6O_{18}$. (a) CV curves at 0.2 mV s^{-1}, (b) rate capabilities, (c) histogram of rate capabilities, and (d) cycling property at 1C.

Fig. 4 CV curves of $MoNb_6O_{18}$ in the voltage ranges (a) 0.8–3.0 V, (b) 1.0–3.0 V and (c) 1.2–13.0 V from 0.2 to 1.0 mV s^{-1}. (d) The slopes of different peak currents after linear fitting in different voltage ranges.

ascribed to the irreversible reaction leading to capacity loss. In contrast, the electrode exhibited a discharge/charge capacity of 219.3/212.4 mA h g^{-1} with an initial Coulombic efficiency as high as 96.8% from 1.0 to 3.0 V. The average charge capacities are displayed in Fig. 3c; the $MoNb_6O_{18}$ electrode exhibited the highest average charge capacity of 198.2 mA h g^{-1} at 0.2C from 1.0 to 3.0 V. However, at a high current density of 5C, it showed the highest average charge at the voltage range 1.2 to 3.0 V, which could be attributed to a more reversible reaction. When the current density returned to 0.2C, the specific capacities almost recovered to their original values for the voltage ranges 1.0 to 3.0 V and 1.2 to 3.0 V, in contrast with a low specific capacity for the range 0.8 to 3.0 V. Determining the cycling stability of the electrode materials is an important way to assess LIBs. Fig. S1 (ESI†) shows the first-cycle voltage profiles at 1C. Three voltage ranges (0.8–3.0, 1.0–3.0 and 1.2–3.0 V) gave first discharge capacities of 145.8, 155.0 and 145.9 mA h g^{-1}, respectively. Cycling performances of an $MoNb_6O_{18}$ electrode at 1C were determined at various voltage ranges, as shown in Fig. 3d. The cycle profile fluctuated to a certain extent, and this fluctuation could be attributed to the environmental differences between daytime and nighttime during the winter, when these experiments were performed. Compared with the other two voltage ranges, the electrode exhibited the highest charge capacity of 137.6 mA h g^{-1} and retention rate of 93% after 60 cycles between 1.0 and 3.0 V. The lithium-storage properties of $MoNb_6O_{18}$ electrode were also compared with those of reported Nb-based and other anodes (Table S1, ESI†).[5,20,24,33,34]

The Li-ion diffusion behavior of the $MoNb_6O_{18}$ electrode was investigated by taking CV measurements of this electrode at the different voltage ranges at various scan speeds from 0.2 to 1.0 mV s^{-1}. As shown in Fig. 4, when the scan rate was increased from 0.2 to 1.0 mV s^{-1}, the reduction and oxidation peaks shifted to lower and higher voltages, respectively. Based
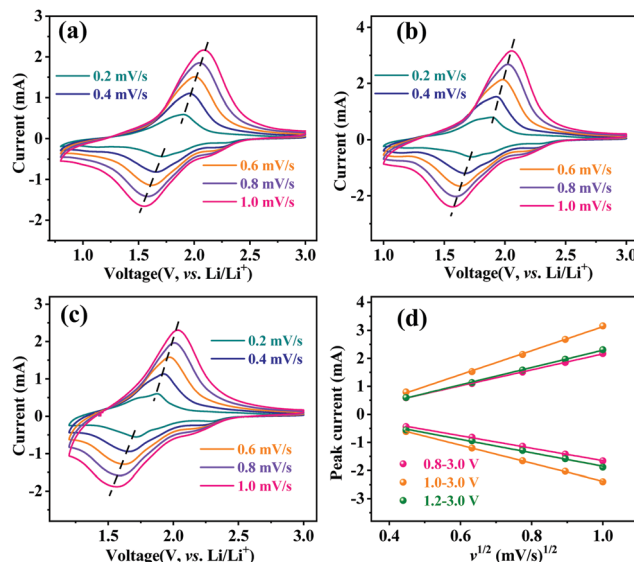
on the linear relationship between the scan rate and peak current (Fig. 4d), the Li-ion diffusion coefficient of the $MoNb_6O_{18}$ electrode was determined by using the Randles–Sevcik equation (eqn (1)).[35]

$$I_p = 2.69 \times 10^5 \times n^{1.5} C_0 S D_{CV}^{0.5} v^{0.5} \qquad (1)$$

In this equation, I_p is peak current, n is the charge transfer number, C_0 is the concentration of Li ions in the electrode, S is the surface area of the electrode, D_{CV} is the Li-ion diffusion coefficient, and v is the scan rate. The calculated D_{CV} values were 1.34×10^{-10}–2.21×10^{-10}, 2.81×10^{-10}–4.99×10^{-10} and 1.56×10^{-10}–2.61×10^{-10} cm^2 s^{-1} for the voltage ranges of 0.8–3.0, 1.0–3.0 and 1.2–3.0 V, respectively. Note that the D_{CV} value for the voltage range 1.0 to 3.0 V was higher than those for the ranges 0.8–3.0 V and 1.2–3.0 V; and it was comparable with those, determined using same method (CV technology), of other intercalation-type niobium-based oxide anode materials such as $MoNb_{12}O_{33}$ (4.0×10^{-14}–8.6×10^{-14} cm^2 s^{-1})[24] and $W_3Nb_{14}O_{44}$ (7.83×10^{-13}–8.02×10^{-13} cm^2 s^{-1}).[27]

The apparent lithium-ion diffusion properties of the $MoNb_6O_{18}$ electrode were further investigated by performing the galvanostatic intermittent titration technique (GITT) during the whole cycle at different voltages (Fig. 5). A current density of 0.1C was applied for 30 minutes to the electrode to control the Li-ion insertion and extraction, following by a relaxation process lasting for 120 minutes. The apparent Li-ion diffusion coefficient (D^{GITT}) values were calculated using the equation[35]

$$D^{GITT} = (4/\pi\tau)(m_B V_m/M_B S)^2 (\Delta E_s/\Delta E_\tau)^2 \quad (\tau \leq l^2/D), \qquad (2)$$

where D^{GITT} is the Li-ion diffusion coefficient in cm^2 s^{-1} determined using GITT, τ is the relaxation time, m_B, M_B, V_m, and S represent, respectively, the mass, molecular weight, molar volume and surface area of the cathode material, ΔE_s
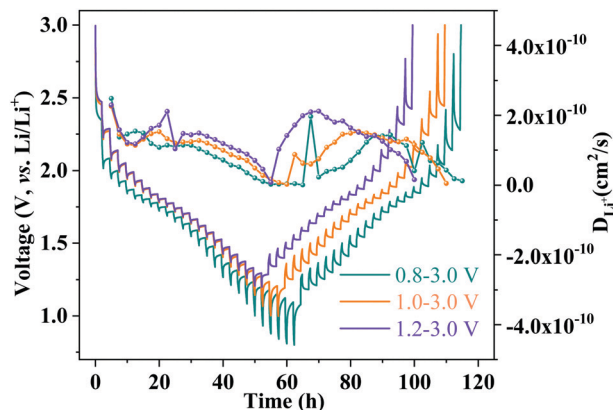
Fig. 5 GITT curves and Li-ion diffusion coefficient profiles of an $MoNb_6O_{18}$ electrode at 0.1C with different voltage windows.

Fig. 7 *Ex situ* XRD patterns of $MoNb_6O_{18}$ electrodes at various voltages.

is the difference between two consecutive stable voltages after relaxation, and ΔE_τ is the transient change in voltage during a single titration step. During the Li-ion insertion/extraction, the ranges of diffusion coefficient (D^{GITT}) values were determined to be 2.48×10^{-10}–6.27×10^{-13}, 2.26×10^{-10}–2.49×10^{-12} and 2.30×10^{-10}–8.41×10^{-12} cm^2 s^{-1} for the voltage ranges 0.8–3.0, 1.0–3.0 and 1.2–3.0, respectively. And the average Li-ion D^{GITT} values were 8.29×10^{-11}, 9.28×10^{-11} and 1.35×10^{-10} cm^2 s^{-1}, respectively. The use of $MoNb_6O_{18}$ yielded faster diffusion of lithium ions than did other niobium-based oxides such as WNb_2O_8 ($\sim 2.8 \times 10^{-11}$ cm^2 s^{-1})[36] and $WNb_{60}O_{153}$ ($\sim 1.51 \times 10^{-14}$ cm^2 s^{-1}).[37]

Electrochemical impedance spectra (EIS) of the $MoNb_6O_{18}$ electrode were acquired with a fresh cell and after 5 cycles at various voltage ranges at 0.2C (Fig. 6). Each Nyquist EIS plot was found to contain a semicircle at the high- to middle-frequency region and a sloping line at the low-frequency region—with the former relevant to the charge-transfer impedance on the electrode–electrolyte interface (R_{ct}), and the latter assigned to the semi-infinite diffusion of lithium ions in the
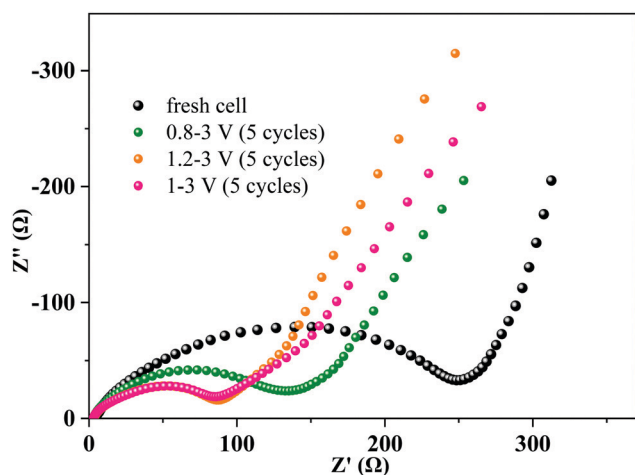
electrode.[38] Interestingly, the diameters of the semicircles at the high to middle frequencies decreased obviously after 5 cycles, revealing an enhancement of the charge-transfer efficiency after cycling. This phenomenon could be attributed to the irreversible insertion of lithium ions into the $MoNb_6O_{18}$ electrode leading to improvement in the electronic conductivity of the electrode.[39,40] The values of the diameters of the semicircle in the voltage ranges 1–3 V and 1.2–3 V were seen to be almost equal and smaller than that of the voltage range 0.8–3 V, indicating that the insertion of lithium ions into the $MoNb_6O_{18}$ electrode occurred most easily in the voltage ranges 1.0–3.0 V and 1.2–3 V.

The structural evolution of $MoNb_6O_{18}$ during charging/discharging at 0.1C was further clarified from the results of an *ex situ* XRD experiment. As shown in Fig. 7, after a full cycle of insertion and extraction of lithium ions, all diffraction peaks almost returned to their original peak positions and recovered their peak intensities, indicating the high reversibility of the lithium ion insertion into/extraction from the structure $MoNb_6O_{18}$. This result verified that $MoNb_6O_{18}$ is an intercalation-type anode material for lithium-ion storage and has outstanding structural stability.

To estimate the potential application of MNO in LIBs, a full battery cell was fabricated with $MoNb_6O_{18}$ as the anode and $LiMn_2O_4$ as the cathode (LMO//MNO).[10,41,42] The working voltage of this LMO//MNO full cell was about 2.0 V (Fig. S2b, ESI†). As shown in Fig. 8, the initial respective charge and discharge capacities of the full cell were 226.2 and 196.3 mA h g^{-1} with a Coulombic efficiency of 86.8% at 0.2C. From the fifth cycle onward, the Coulombic efficiency was above 98%, indicating a highly reversible charge/discharge process. After 30 cycles, the full cell maintained a discharge capacity of 152 mA h g^{-1}. The properties of the full cell were comparable to those of an $LiMn_2O_4$// porous $MoNb_{12}O_{33}$ microsphere full cell (~ 170 mA h g^{-1} at 1C after 100 cycles)[24] and $LiMn_2O_4$//nanowire $Mo_3Nb_{14}O_{44}$ full cell

Fig. 6 Nyquist plots of $MoNb_6O_{18}$ in the voltage ranges 0.8–3.0, 1.0–3.0 and 1.2–3.0 V.

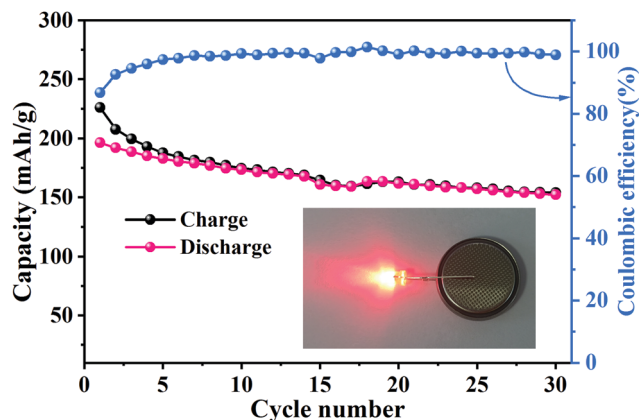**Fig. 8** Cycling properties and Coulombic efficiency levels of an LMO//MNO full cell at 0.2C; inset: red-LED powered by the LMO//MNO full cell after 30 cycles.

(201 mA h g^{-1} at 0.1C, 73 mA h g^{-1} at 5C after 500 cycles).[33] A red-LED (Fig. 8 inset) was successfully powered by the LMO//MNO full cell after 30 cycles, certifying the potential practicability of the full cell. The excellent results for this full cell revealed that $MoNb_6O_{18}$ has potential applications in LIBs.

Conclusions

In summary, $MoNb_6O_{18}$ was investigated as a new intercalation-type anode material for LIBs. Pure-phase micro-scale $MoNb_6O_{18}$ was fabricated using a simple solid-state method with MoO_3 and Nb_2O_5 as raw materials. $MoNb_6O_{18}$ formed a monoclinic shear ReO_3-type crystal structure in the space group $I2/m$, consisting of a $(3 \times 4)_\infty$ NbO_6 octahedron block and an MoO_4 tetrahedron at the corner of the block. In the half-cells, the $MoNb_6O_{18}$ electrode operated at a safe voltage (of about 1.72 V) and showed a reversible capacity of up to 219.4 mA h g^{-1} at 0.2C and 154.3 mA h g^{-1} at 1C in the voltage range 1.0 V to 3.0 V. Moreover, the $LiMn_2O_4$//$MoNb_6O_{18}$ full cell delivered charge and discharge capacities of 226.2 and 196.3 mA h g^{-1} at 0.2C with an energy density of 393 W h kg^{-1}. Due to its multi-electron reactions, safe operating voltage, and reversible crystal structural evolution, $MoNb_6O_{18}$ is expected—in particular after subjecting it to morphology optimization, nano-sizing and carbon synergy—to be a competitive candidate anode material for large-scale energy storage systems, especially in EVs. Also, this work has provided some new insights for investigations of M–Nb–O mix-oxides used as anode materials for LIBs.

Conflicts of interest

The authors declare no conflict of interest.

Acknowledgements

References

1 R. Schmuch, R. Wagner, G. Hörpel, T. Placke and M. Winter, *Nat. Energy*, 2018, **3**, 267–278.
2 X. Hu, S. E. Li and Y. Yang, *IEEE Trans. Transp. Electrif.*, 2017, **2**, 140–149.
3 B. Alex, W. Lars, T. Andrea and T. Axel, *J. Cleaner Prod.*, 2018, **89**, 292–308.
4 S. J. Kim, H. C. Park, M. C. Kim, D. M. Kim, Y. W. Lee and K. W. Park, *J. Power Sources*, 2015, **273**, 707–715.
5 C. Wei, H. Fei, Y. Tian, Y. An, Y. Tao, Y. Li and J. Feng, *Chin. Chem. Lett.*, 2020, **31**, 980–983.
6 Z. Luo, C. Liu and S. Fan, *J. Mater. Chem. A*, 2019, **7**, 3642–3647.
7 M. Armand and J. M. Tarascon, *Nature*, 2008, **451**, 652–657.
8 R. Srinivasan and L. Srinivasan, *J. Power Sources*, 2015, **293**, 876–882.
9 J. B. Goodenough and Y. Kim, *J. Power Sources*, 2011, **196**, 6688–6694.
10 Z. Zhang, Y. Huang, X. Li, S. Zhang, Q. Jia and T. Li, *Chem. Eng. J.*, 2021, **421**, 129827.
11 S. I. Choi, E. J. Jung, M. Park, H. S. Shin and S. W. Yong, *Appl. Surf. Sci.*, 2020, **508**, 145237.
12 T. Yi, S. Yang and X. J. Ying, *J. Mater. Chem. A*, 2015, **3**, 5750–5777.
13 G. Hao, L. Ning, D. Li, C. Dai and D. Wang, *J. Phys. Chem. C*, 2009, **113**, 6324–6326.
14 S. Lee, W. Eom, H. Park and T. H. Han, *ACS Appl. Mater. Interfaces*, 2017, **9**, 25332–25338.
15 K. Kanamura, T. Umegaki, H. Naito, Z. Takehara and T. Yao, *J. Appl. Electrochem.*, 2001, **31**, 73–78.
16 D. Yoshikawa, Y. Kadoma, J. M. Kim, K. Ui, N. Kumagai, N. Kitamura and Y. Idemoto, *Electrochim. Acta*, 2010, **55**, 1872–1879.
17 T. Tomohiro, Y. Shinpei, F. Yuki, A. Kengo, U. Kotaro, I. Ryoji and S. Yoji, *J. Electrochem. Soc.*, 2018, **165**, A1231–A1237.
18 Q. Fu, X. Zhu, R. Li, G. Liang, L. Luo, Y. Chen, Y. Ding, C. Lin, K. Wang and X. Zhao, *Energy Environ. Mater.*, 2020, **30**, 401–411.
19 Y. Yang and J. Zhao, *Adv. Sci.*, 2021, 2004855.
20 L. Qin, Y. Liu, S. Xu, S. Wang, X. Sun, S. Zhu, L. Hou and C. Yuan, *Small Methods*, 2020, **4**, 2000630.
21 Q. Deng, Y. Fu, C. Zhu and Y. Yu, *Small*, 2019, **15**, 1804884.
22 R. S. Roth and A. D. Wadsley, *Acta Crystallogr.*, 1965, **19**, 26–32.
23 K. J. Griffith, K. M. Wiaderek, G. Cibin, L. E. Marbella and C. P. Grey, *Nature*, 2018, **559**, 556–563.
24 X. Zhu, J. Xu, Y. Luo, Q. Fu, G. Liang, L. Luo, Y. Chen, C. Lin and X. S. Zhao, *J. Mater. Chem. A*, 2019, **7**, 6522–6532.
25 A. D. Saritha, B. V. Pralong, A. U. V. Varadaraju and B. B. Raveau, *J. Solid State Chem.*, 2010, **183**, 988–993.
26 X. Ma, P. Chen, M. Qian, D. Wu, J. Du, X. Chen, R. Dai, M. Sha, Z. Zi and J. Dai, *J. Alloys Compd.*, 2021, **864**, 158379.
27 Y. Yang, H. Zhu, J. Xiao, H. Geng, Y. Zhang, J. Zhao, G. Li, X. Wang, C. Li and Q. Liu, *Adv. Mater.*, 2020, **32**, 1905295.

28 K. J. Griffith, I. D. Seymour, M. A. Hope, M. M. Butala, L. K. Lamontagne, M. B. Preefer, C. P. Koçer, G. Henkelman, A. J. Morris, M. J. Cliffe, S. E. Dutton and C. P. Grey, *J. Am. Chem. Soc.*, 2019, **141**, 16706–16725.

29 S. Deng, Y. Zhang, D. Xie, L. Yang, G. Wang, X. Zheng, J. Zhu, X. Wang, Y. Yu, G. Pan, X. Xia and J. Tu, *Nano Energy*, 2019, **58**, 355–364.

30 X. Ma, L. Cheng, L. Li, X. Cao, Y. Ye, Y. Wei, Y. Wu, M. Sha, Z. Zi and J. Dai, *Electrochim. Acta*, 2020, **332**, 135380.

31 C. Yang, S. Yu, C. Lin, F. Lv, S. Wu, Y. Yang, W. Wang, Z. Zhu, J. Li, N. Wang and S. Guo, *ACS Nano*, 2017, **11**, 4217–4224.

32 U. K. Sen, A. Shaligram and S. Mitra, *ACS Appl. Mater. Interfaces*, 2014, **6**, 14311–14319.

33 R. Li, G. Liang, X. Zhu, Q. Fu, Y. Chen, L. Luo and C. Lin, *Energy Environ. Mater.*, 2021, **4**, 65–71.

34 X. Yang, Y. Wang, B. Hou, H. Liang, X. Zhao, H. Fan, G. Wang and X. Wu, *Acta Metall. Sin. (Engl. Lett.)*, 2021, **24**, 390–400.

35 A. J. Bard and L. R. Faulkner, *Russ. J. Electrochem.*, 2002, **38**, 1364–1365.

36 Z. Zhou, S. Lou, X. Cheng, B. Cui and G. Yin, *ChemistrySelect*, 2020, **5**, 1209–1213.

37 Q. Tian, W. Ye, H. Yu, X. Cheng, H. Zhu, N. Long, M. Shui and J. Shu, *Ceram. Int.*, 2019, **45**, 1893–1899.

38 F. Lu, Q. Chen, S. Geng, M. Allix, H. Wu, Q. Huang and X. Kuang, *J. Mater. Chem. A*, 2018, **6**, 24232–24244.

39 R. Song, H. Song, J. Zhou, X. Chen, B. Wu and H. Y. Yang, *J. Mater. Chem.*, 2012, **22**, 12369–12374.

40 H. Chen, L. X. Ding, K. Xiao, S. Dai, S. Wang and H. Wang, *J. Mater. Chem. A*, 2016, **4**, 16318–16323.

41 Y. Wang, B. Hou, J. Guo, Q. Ning, W. Pang, J. Wang, C. Lv and X. Wu, *Adv. Energy Mater.*, 2018, **8**, 1703252.

42 B. Hou, Y. Wang, J. Guo, Y. Zhang, Q. Ning, Y. Yang, W. Li, J. Zhang, X. Wang and X. Wu, *ACS Appl. Mater. Interfaces*, 2018, **10**, 3581–3589.